Indian Journal of Pure & Applied Physics
Vol. 64, February 2026, pp. 197-208
DOI: 10.56042/ijpap.v64i2.25940

Intelligent Fault Detection in PSO-MPPT based Photovoltaic and Electric Vehicle Integrated System Under Partial Shading Conditions

S Venkata Ramudu Naik* & Pulivarthi Nageswara Rao

Department of Electrical Electronics and Communication Engineering, GITAM school of technology GITAM (Deemed to be University) Visakhapatnam 530 045, India

Received: 26th November 2025; accepted: 12th January 2026

A method to amend the operation of a Photovoltaic (PV) system plus Electric vehicles (EVs) integrated system, under varied partial shading conditions and varying irradiance conditions using an optimized Maximum Power Point Tracking (MPPT) technique. As solar energy becomes more popular, it's crucial to optimize PV panel efficiency to meet growing demand. Nevertheless, PV panels face challenges, including Partial Shading Conditions (PSCs), which significantly impacts their efficiency. In this study, Particle Swarm Optimization (PSO) algorithm based MPPT is used to calculate the Global Maximum peak point (GMPP) from peak power measurements and an improved grid management scheme based on a Novel Convolutional Neural Network (NCNN) was developed and trained using an Enhanced Golden Search Algorithm (EGSA). EGSA can adjust hyperparameters effectively, which promotes model performance and accelerates the convergence rate. Partial shading-induced faults are identified with high sensitivity, and a diagnosis accuracy of 99.6 % and a fast response time of 0.45 s are obtained. With the help of Simulation results the efficacy of the propositioned method is tested and validated.

Keywords: Photovoltaic, Electric vehicle, Particle swam optimization, Partial shading

1 Introduction

The drive for untainted energy and a decline in fossil-fuel reserves has prompted a shift from the traditional power grid to a renewable energy-based generating system. There has been a worldwide revolution in the adoption of green energy over gas-based energy bases, as they are cited as primary contributors to Green-House-Gas (GHG) emanations and global warming. Almost every country in the world is accentuating the reduction of GHG emissions. Ensuing the GHG emission reduction objective, utmost countries have established renewable usage to counterbalance the equivalent generation from traditional fossil-fuel-based power plants. Variety of green energy bases are interconnected into the electricity network. Amid all other renewable energy options, wind and PV systems are widely utilized. PV is particularly favored due to its straightforward installation, availability, and quiet operation, making it commonly adopted for integrated power grid distribution networks. The intermittent nature of solar PV systems results in variable power injection into the grid, driven by the availability of solar irradiance[1]. Unlike conventional energy sources, which can adjust output to match load demand, PV generation cannot be directly controlled to align with consumption needs. This introduces new dynamics to power network operations, and large-scale adoption of PV can create significant challenges for maintaining grid stability[2]. Beyond fossil-fuel-based power plants, the automotive sector represents to GHG emanations in both developed and developing nations. To reduce this, recent vehicle development has shifted toward EVs using electric motors and battery storage[3]. EVs are becoming cheaper as battery technology advances and battery prices fall. Furthermore, the distance travelled with a single charge is currently like gas-based vehicles. The demand for EVs is increasing due to low life cycle costs. High incursion green energy in the power grid, as well as EV adaptation, are critical to ensuring long-term energy infrastructure and a decarbonized environment[4].

Partial shade, rapidly changing solar irradiance, bidirectional power flow, and non-uniform EV charging load patterns are some of the dynamic operating conditions and Variations in power quality can disrupt voltage control and induce frequency deviations, making it difficult to maintain voltage levels in real-time settings. Machine Learning (ML) and Deep Learning (DL) are promising methodologies for intelligent data understanding and

*Corresponding author: E-mail: vsugali@gitam.in

system decision-making. These algorithms are effective for fault type detection, load prediction, renewable energy forecasting, and grid state estimation/monitoring. However, there are several issues that could make connecting PV-EV to the grid challenging, including as Power Quality Disturbances (PQDs). The nonlinear multivariate character of the renewable-based microgrid will not be met by traditional fault detection techniques including rule-based, model-based, and statistical-based techniques. They might be rigid, costly to compute, and unable to adjust to changing surroundings.

On the other hand, when it comes to taking use of the spatial-temporal correlations and underlying patterns of the system electrical response, data-driven models especially those based on Convolution Neural Network (CNN) offer a more efficient learning framework. Metaheuristic optimization methods, including Lyrebird Optimizer, Energy Valley Optimizer, and golden search-based algorithms, have been used to enhance hyperparameter tuning, training convergence, and model generalization in fault-detection network. This study builds on previous research by incorporating an innovative NCNN model into the Grid Optimization and Fault Detection Model (GO-FDM). The optimization rule is constructed using EGSA, which adjusts critical parameters based on convergence rate and deep learning.

A straightforward control technique for an isolated electric car charging station energized by a PV arrangement is presented[5]. The structure is made up of three primary regulators the intelligent MPPT controller, the battery charge controller, and the battery management. The controller ensures that the PV array operates at its MPP, and the battery controller and management system govern the Energy Storage System (ESS) and EV charging and discharging operations, respectively.

The portrayed scheme also features a basic Energy Management System (EMS) to properly regulate energy flow in the interior system. The application of Model Predictive Control (MPC) in a microgrid system made up of PV electricity and EV battery chargers is investigated[6]. By considering battery State of Charge (SoC), the MPC technique abridged day-to-day grid crest power by 59 %, proving its efficacy in crowning strip and energy balance. Likewise[7], an MPC co-optimization structure for PV-EV-hydrogen systems that stemmed in a 12 % drop in system losses and a 53 % increase in EV consumer ease. An optimization strategy employing a Modified Snake Optimization (MSO) procedure for the financial scaling of a grid-associated PV-battery-operated system for quick EV chargers is developed[8]. The research emphasized the redeemable efficient power flow amid PV panel, battery pack, and the grid, which adds to the monetary feasibility of PV-EV systems. A detailed analysis was conducted that considered various PV network topologies corresponding, Series, Parallel configurations, combination of both series-parallel, BL, TCT, and HC in all shadowing instances[9]. The functioning and output topographies of different combinations are studied and interrelated over a variety of shading circumstances. The TCT arrangement performs better in most PSC scenarios. TCT setup unable to deliver the extreme feasible power in partial shadowing, and the obtained output power can be enhanced further.

A different approach has recently been used to maximize power output in non-optimal irradiation situations[10]. One of the best ways to reduce the adverse effects of PSCs and increase the power collected from PV modules is the PV rearrangement process. Equalizing the currents generated by countless electrical rows is its primary goal. If not, the reconfiguration procedure involves moving the PV panels that are electrically or physically connected to balance the irradiance. PSO to trace the GMPP in shadowing instances is proposed[11]. The functioning was evaluated by means of simulation and instigated in grid integrated PV systems that custom a DC-DC converter to follow the global optimum. The Power-Current (P-I) curve is utilized to implement MPPT. The results disclose that the MPPT algorithm was successful in tracking the GMPP under both uniform and varied insolation situations. An advanced PSO method that minimizes the weighting factor of the particle, cognitive coefficients, and social aspects, to accelerate concurrence is discussed[12]. This method was applied in Simulink environment, and the outcome demonstrate that steps were abridged while convergence time improved.

Compared to many recent algorithms, PSO offers faster convergence with fewer control parameters, making it suitable for practical implementation under dynamically changing partial shading conditions. Moreover, the primary contribution of this study lies in the proposed system framework and fault detection strategy rather than in introducing a new optimization algorithm.

The NCNN-EGSA system aims to detect faults in PSO MPPT based PV-EV distribution networks with high accuracy and low latency, while also optimizing grid stability in real-time based on changing solar power and EV demand. A PV-EV integrated system is modelled by using Simulation tool. The recommended algorithm's performance is verified by subjecting the modeled system to various irradiation patterns.

2 Integrated PV and EV System

2.1 PV System

The PV and EV are mutually connected to the electricity grid, and the overall effect might vary depending on their connection and running period. There are various options for integrating PV and EV hooked on the grid, and the PV and EV connection point in the grid is determined by the voltage magnitude at the assembly point. Large-scale solar power plants and EV load collectors are frequently linked to medium-voltage network and high-voltage transmission systems. Rooftop PVs are becoming increasingly popular in families, also in small and medium-sized business buildings on the distribution grid[13,14]. Furthermore, as personal EVs become more popular[15], they are allied to the low voltage network while vehicle is charging as shown in the Fig. 1. The analytical procedures that are primarily used by researchers are explained here.

The electrical equivalent circuit describes the PV cell, which has various unknown factors. These factors are used calculated by combining arithmetic formulae with ecological input variables like solar irradiance and its temperature. The single diode model is made up of a dependent current source, a diode that characterizes the diffusion current factor, and a series connected resistance that compensates for the power losses produced by device resistance, external contacts, and additional line interconnectedness amid individual PV cell and module. Figure 2 represents a typical PV cell model[16,17].

The electrical circuit of the solar cell, as shown in Fig. 2, includes a parallel resistance (RP) to account for leakage current, crystal defects, and impurities. Therefore, the Eq. (6) is rewritten as,

$$I = I_{pv} - I_o \left[exp\left(\frac{V+IR_S}{aV_t} - 1\right)\right] - \frac{V+IR_S}{R_P} \quad \ldots (1)$$

where RP is the parallel resistance.

Since multiple PV elements allied in series and parallel, Eq. (1) is modified as

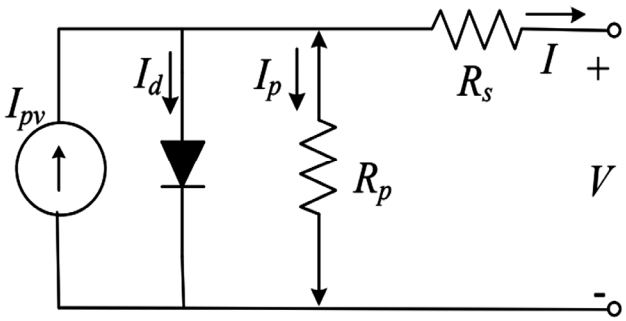

Fig. 2 — The PV cell using single diode model with shunt resistance

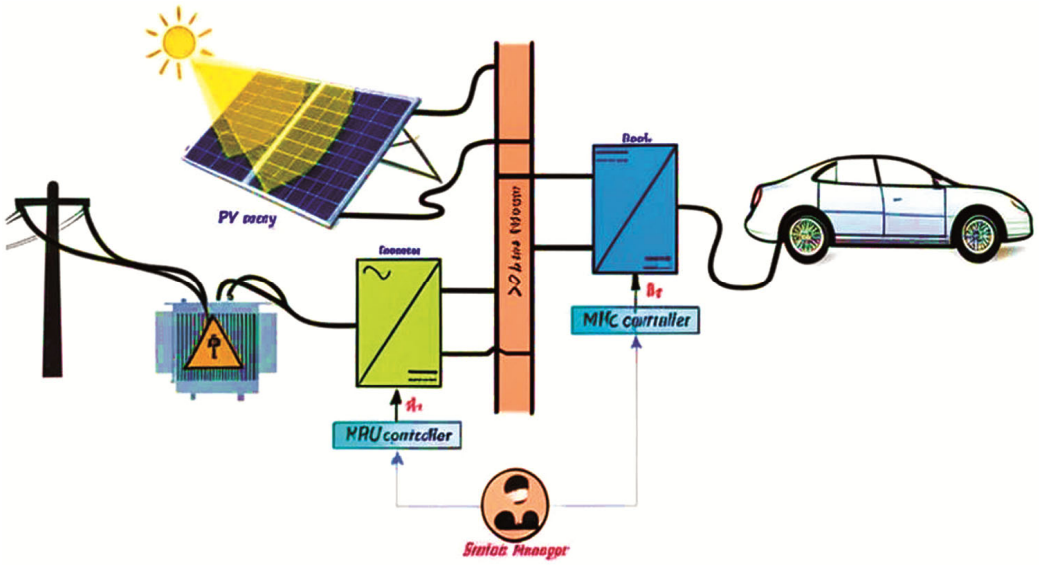

Fig. 1 — Typical PV+EV integrated system

$$I = I_{pv}N_{pp} - I_o N_{pp}\left[exp\left(\frac{V+\lambda IR_s}{aN_s V_t N_{ss}}\right) - 1\right] - \frac{V+\lambda IR_s}{\lambda R_P} \quad \ldots (2)$$

While related to the single diode model and two diode model is more precise it includes the series connected resistance power losses and additional leakage current. Adds another diode in parallel with the preceding five-parameter model to replicate the power losses triggered by the carrier rejoining in the space charge region of the junction and exterior rejoin[18]. The electrical circuit of two diode type is shown in Fig. 3.

The current equation is calculated as,

$$I = I_{pv} - I_{o1}\left[exp\left(\frac{V+IR_s}{a_1 V_t}\right) - 1\right] - I_{o2}\left[exp\left(\frac{V+IR_s}{a_2 V_t}\right) - 1\right] - \frac{V+IR_s}{R_P} \quad \ldots (3)$$

where I_{01} and I_{02} are the reverse-saturation currents of individual diodes, and a_1 and a_2 are the ideality-factors of each diode, the above equation is formed for a PV array with additional coefficients as,

$$I = N_{pp}I_{pv} - N_{pp}I_{o1}\left[exp\left(\frac{V+\lambda IR_s}{a_1 V_t N_{ss} N_s}\right) - 1\right] - N_{pp}I_{o2}\left[exp\left(\frac{V+\lambda IR_s}{a_2 V_t N_{ss} N_s}\right) - 1\right] - \frac{V+\lambda IR_s}{\lambda R_P} \quad \ldots (4)$$

Extensive PV systems are often allied to medium-voltage radial lines using step-up transformers as shown in Fig. 4. Inverters tied to PV systems deliver low short-circuit current to grids with zero mechanical inertia. A PSO based MPPT controller energies the DC/DC converter in a PV structure to exploit power output from PV panels. In short, the DC/AC converter controller acts in accordance with the mode of action of the PV. In the grid-integrated PV system, the DC/AC converter controller's goal is to send as much solar electricity as feasible to the grid[19].

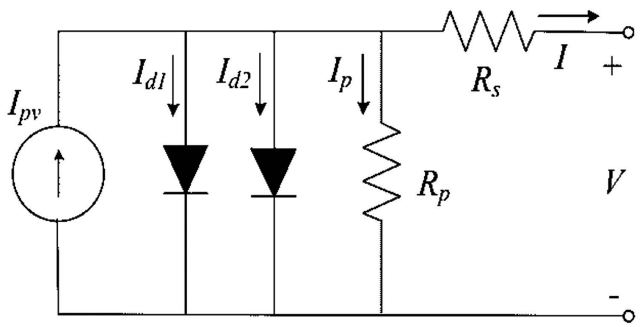

Fig. 3 — The two-diode model with shunt resistance

2.2 EV System

The EV system consists of a battery pack, a bi-directional DC-DC converter, a motor controller, a three-phase inverter, and a motor attached to the wheels. The battery is a vital source of energy, represented by an analogous circuit that consists of a voltage source and resistance, as shown below.

$$V_{batt} = V_{oc} - I_{batt} \times R_i \quad \ldots (5)$$

where V_{batt} is the terminal voltage, V_{oc} is the open-circuit voltage, I_{batt} is the battery current, and R_i is the internal resistance. The DC-DC converter controls the terminal voltage level amid the battery and the three-phase inverter and thus enables both charging and discharging purposes. The inverter alters the DC signal into a three-phase AC for motor that propels the wheels, the torque produced by the motor is given by,

$$T = \frac{P_m}{\omega_{shaft}} \quad \ldots (6)$$

where T is the motor torque, and P_m is the motor output power, and ω_{shaft} is the motor shaft angular velocity. When gliding, the motor act as a generator that recharges the battery with electrical energy previously supplied by the battery. Also, the State of Charge (SoC) of the battery cell is a significant dynamic variable from an energy management perception and is given as,

$$SoC(t) = SoC(t_o) - \frac{1}{c_{bat}}\int_{t_o}^{t} I(t)dt \quad \ldots (7)$$

where C_{batt} is the capacity of the battery and $I_b(t)$ is the current at time t. The EV load is calculated as:

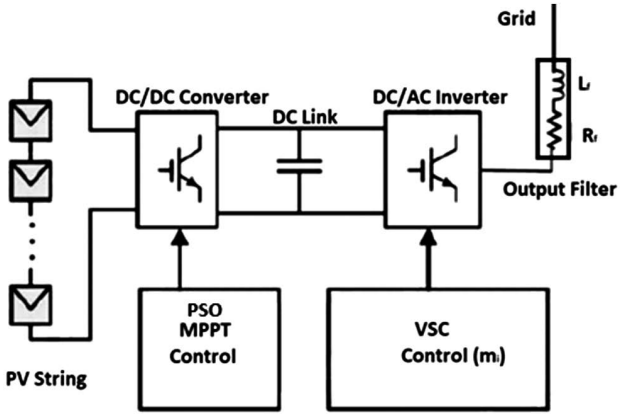

Fig. 4 — PV System control blocks

$$P_{ev} = V \times I = \eta_{inv} \times \eta_{mot} \times P_{batt} \quad \ldots (8)$$

where V and I represents battery terminal voltage and current correspondingly. η_{inv} and η_{motor} are efficiencies of the inverter and motor respectively. Because the EV will be treated as a single entity rather as a PV unit, ESS, and many EVs, the scope of the power coordination problem will be reduced.

2.3 PV under PSCs

The model of a series-connected PV array under PSCs shown in Fig. 5, describes how shading affects the electrical performance of the array. In a series configuration, all modules carry the same current, but partial shading on one or more modules reduces their power generation, creating a mismatch in the array. This mismatch can lead to a drop in overall power output, reverse voltage biasing in shaded modules, and the formation of hotspots, which can cause long-term impairment. To mitigate these problems, by-pass diodes are often incorporated into the elements, allowing current to bypass shaded sections and prevent excessive power losses. However, bypass diode activation alters the current-voltage characteristics, creating multiple peaks in the power curve, which makes MPPT more complex. The impact of shading depends on factors such as the position, intensity, and distribution of the shaded areas.

Modelling the conduct of a series-connected PV array under shadowing helps in designing reconfiguration strategies, optimizing MPPT techniques, and improving overall system efficiency. The terminal current of the two series connected PV modules is given as

$$I = \alpha I_{pv} - I_o \left[exp\left(\frac{V+2IR_S}{2aV_t} - 1\right)\right] - \frac{V+2IR_S}{2R_P} \quad \ldots (9)$$

The model of a parallel-connected PV scheme under PSCs shown in Fig. 6, examines how shading affects the electrical performance when PV elements are allied in parallel. In this formation, each module

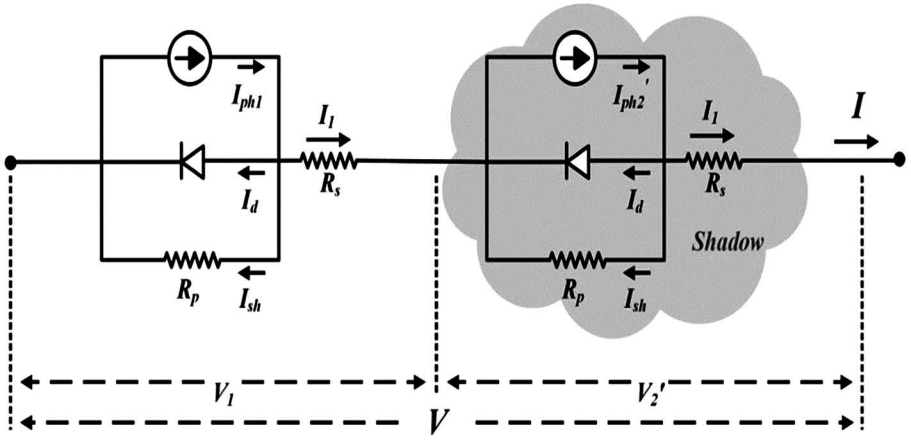

Fig. 5 — Series PV array under PSCs

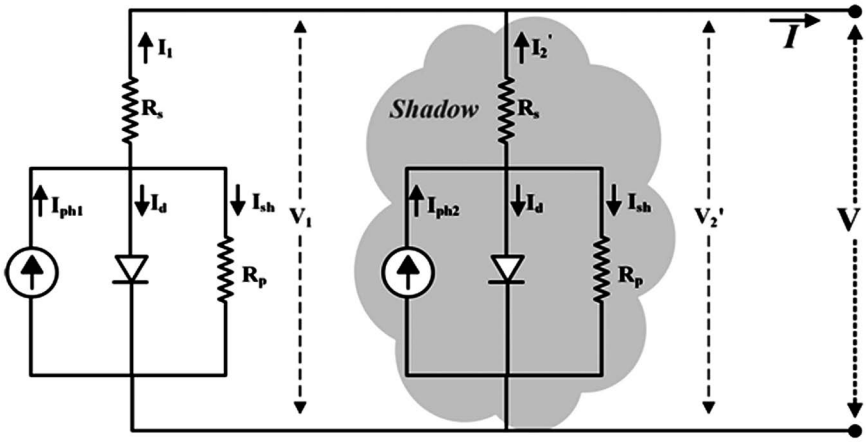

Fig. 6 — Parallel PV array under PSCs

operates at its own voltage, while the total current is the summation of the currents generated by specific elements. Under shadowing, the shaded modules generate less current than unshaded ones, causing an imbalance in power distribution.

Unlike series-connected arrays, where shading on one module can significantly reduce the overall output, a parallel configuration minimizes the impact of shading by allowing unshaded modules to operate at their maximum potential. However, differences in voltage among modules can lea ad to circulating currents, increasing power losses, and reducing efficiency. To address these issues, MPPT controllers and power optimizers are used to ensure optimal power extraction from each module.

Understanding the conduct of a parallel-connected PV array under shadowing is essential for improving energy yield, designing efficient power management systems, and minimizing losses in photovoltaic applications. The two number of parallel-connected PV modules in the array, the output current under PSC is expressed as,

$$I = I_{pv1} + I_{pv2}' - 2I_o\left[exp\left(\frac{2V+IR_S}{2aV_t}-1\right)\right] - \frac{2V+IR_S}{R_P} \quad \ldots (10)$$

$$I = I_{pv0} + \alpha I_{pv0} - 2I_o\left[exp\left(\frac{2V+IR_S}{2aV_t}-1\right)\right] - \frac{2V+IR_S}{R_P} \quad \ldots (11)$$

$$I = (1+\alpha)I_{pv0} - 2I_o\left[exp\left(\frac{2V+IR_S}{2aV_t}-1\right)\right] - \frac{2V+IR_S}{R_P} \quad \ldots (12)$$

Understanding the conduct of a series-parallel PV array under shadowing is crucial for designing efficient solar power systems with enhanced reliability and performance. The output current from SP configuration if any one of the modules is under PSC are expressed as,

$$I = I_{pv1} - I_o\left[exp\left(\frac{V_1+I_1R_S}{aV_t}-1\right)\right] - \frac{V_1+I_1R_S}{R_P} + I_{pv2}' - I_o\left[exp\left(\frac{V_2+I_2R_S}{aV_t}-1\right)\right] - \frac{V_2+I_2R_S}{R_P} \quad \ldots (13)$$

$$I = I_{pv1} + I_{pv2}' - 2I_o\left[exp\left(\frac{V+IR_S}{2aV_t}-1\right)\right] - \frac{V+IR_S}{R_P} \quad \ldots (14)$$

$$I = I_{pv0} + \alpha I_{pv0} - 2I_o\left[exp\left(\frac{V+IR_S}{2aV_t}-1\right)\right] - \frac{V+IR_S}{R_P} \quad \ldots (15)$$

$$I = (1+\alpha)I_{pv0} - 2I_o\left[exp\left(\frac{V+IR_S}{2aV_t}-1\right)\right] - \frac{V+IR_S}{R_P} \quad \ldots (16)$$

3 Intelligent Controllers

Intelligent MPPT techniques, and power electronics solutions are crucial to optimizing PV array performance under varying shading conditions, Fault Detection in PV +EV Integrated Systems with Partial Shade.

To acquire local and global searches, exploration and exploitation should be balanced as much as possible. Local searches in the current place are also important for exploitation. Furthermore, they differ from one another in that one may sacrifice the other when improvising.

Therefore, finding the ideal balance between exploitation and exploration is a challenging and important problem for any optimization algorithm[20]. Thus, the following are a few of the limitations of GSO

(i) This approach is simple to use and maintains a constant population size for each generation. However, this reduced the versatility of the algorithm.
(ii) It becomes stuck in local optima and does not respond robustly when attempting to achieve global optimization for various functions.
(iii) It has both effective local exploitation capabilities and weak exploitation.

The proposed NCNN algorithm is designed with a shallow architecture and a limited number of convolutional layers, which significantly reduces computational complexity compared to deep CNN models.

The dominant operations consist of convolution and activation functions, whose computational complexity scales linearly with the input feature size and the number of kernels, i.e., $O(N{\cdot}K)$, where N represents the number of input samples and K denotes the number of convolution filters. Since the NCNN processes low-dimensional electrical signals (voltage, current, and power) rather than high-resolution images the overall computational burden remains low and is well suited for real-time deployment in PV+EV integrated systems.

EGSO is designed with disadvantages in mind. The starting population is created using opposite functions.

Reverse solutions are produced using an oppositional function. This function provides the best NCNN hyperparameter solutions while also improving the original population. The search process starts with an initial random generation of candidate solutions using the GSO a population-based metaheuristic optimization technique. This algorithm considers the step size variable and upgrades the object positions in each iteration until the compensated termination condition. The proposed NCNN approach achieves the highest accuracy with the lowest response time among the compared methods, demonstrating rapid convergence and superior adaptability under partial shading and dynamic EV loading conditions shown in Table 1.

To capture the spatial and temporal information of the basis features voltage waveform, current level, and irradiation value the proposed defect detection model employs a unique NCNN. The EGSA is used to adjust the hyperparameters of the suggested model to boost training accuracy and generalization capacity. With a response time of 0.45 seconds, this approach has a defect detection accuracy of 99.6 %. By analyzing the streams of data gathered from the smart sensors in real time and sending them to the trained NCNN-EGSA model at the edge or cloud, real-time defect diagnosis is made easier. When a mistake occurs, the system generates notifications and takes automatic corrective action. And the PSO process is a practice stimulated by the communal behavior of public insect clusters and supplementary mammal societies. The PSO moves every particle through the space search, amending the finest answer found by the experience of its neighbors. The PSO begins by arbitrarily initializing particles, then iteratively looking for optimal results and estimating resolution using a fitness function. The PSO process searches for global optimums with great accuracy. The locus of the finest particle in a neighborhood influences the particle's location. The particle location is altered using (17).

$$X_i^{t+1} = X_i^t + V_i^{t+1} \quad \dots (17)$$

Each iteration is characterized by the velocity factor, Vi, and is obtained using (18).

$$V_i^{t+1} = \omega . V_i^t + c_1 r_1 \left(P_{best_i} - X_i^t\right) + c_2 r_2 \left(g_{best_i} - X_i^t\right) \quad \dots (18)$$

where i=1,2,…n, denotes the particle to be augmented, t = total iterations, Vit and Xit are velocity and location of the ith particle within kth iterations, $Pbesti$ archives the individual best location of the ith particle, $gbesti$ archives the global best location in the swarm, w = inertia of the particle, $c1$ & $c2$ are cognitive coefficient of specific particles, $r1$ & $r2$ are random values (0,1) of dimension (1 X D) and D is the amount of decision particles velocity.

The optimization algorithm comprises stages such as the exploitation and exploration stages. It is also maintaining the equilibrium between two contradicting functions. The two primary components of this optimization technique are the process of updating the position creating a population and evaluating fitness. EGSA was employed to optimize the hyperparameters. As shown in Fig. 7, the stages of the process are as follows

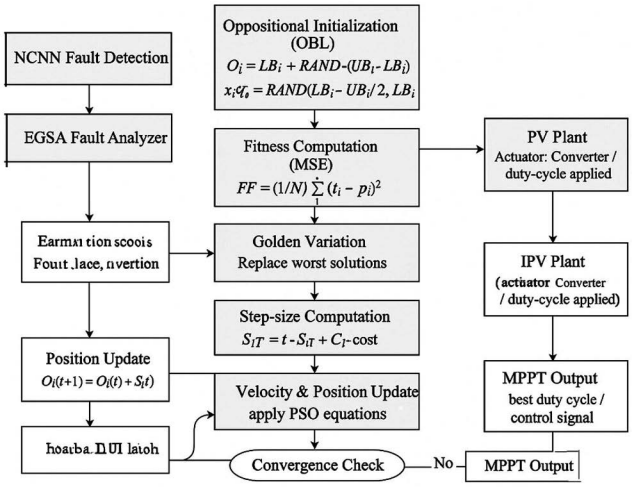

Fig. 7 — Stages of proposed algorithm

Table 1 — Comparative Performance Analysis

Method	Accuracy (%)	Response Time (ms)	Convergence Speed	Remarks
PSO-based MPPT	94.5	25–35	Moderate	Sensitive to parameter tuning;
GWO-based MPPT	95.8	18–25	Fast	Improved exploration but higher computational load
GOA-based MPPT	96.2	20–28	Fast	Good global search, may exhibit oscillations
Conventional CNN	97.5	12–18	Fast	High accuracy but increased computational complexity
Proposed NCNN (PSO-Optimized)	99.6	6–10	Very Fast	Low complexity, robust under PSCs, suitable for real-time PV+EV systems

3.1 Initialization with Oppositional

To obtain the best global search results, this method uses a quasi-opposition function. This algorithm begins the search process with two arbitrarily generated objects in the search space that are connected as follows,

$$O_i = LB_i + RAND\,.(UB_i - LB_i); i = 1,2,3,\dots n \quad \dots (19)$$

$$x_i^{Q0} = RAND\left(\frac{LB_i - UB_i}{2}, LB - x_i\right), i = 1,2,3\dots pop \quad \dots (20)$$

Here, $UB_i\ and\ LB_i$ is the lower and upper bounds, respectively. The positions of the objects within the search space are denoted by O_i and Solution based on quasi-oppositional functions is denoted by x_i^{Q0}.

3.2 Fitness Computation

This step involves computing the starting population in relation to the objective function and selecting the object with the best fitness value. A fitness function was used to train and validate the proposed model. The low parameters of the utility function show how well the model's predictions for facial remarks match the reality. Therefore, the fitness function calculates the forecast accuracy. The Mean Square Error is aimed at the fitness function.

$$FF = \frac{1}{N}\sum_{i=1}^{N}(t_i - p_i)^2 \quad \dots (21)$$

Here, the total number of features is N. p_i is the definition of the expected parameters and the true parameters are represented by t_i.

3.3 Golden Variation

The third stage involves sorting items according to their fitness function and changing the object with the lowest fitness using a random solution.

3.4 Step Size Computation

The step size operator is considered in each iteration of the optimization process to modify the objects to the ideal solution. There are three components of the step size operator. In the first part, the transformer operator which reduces iteratively to balance the algorithm's local and global search estimates the previous variable of the step size, which is different. The distance between the object's current location and its best position to date was determined by calculating the cosine of a random parameter in the range of 0 to 1. Finally, the sine of a random parameter between d and 1 is multiplied to determine the distance between the current position of the ith, object and the ideal position attained thus far among all objects. The step size operator is generated at random in the first optimization iteration and updated using the following equations as needed.

$$S_{Ti}(T+1) = t.S_{Ti}(T) + C_1.Cos(R_1).(Obest_i - x_i(t) + C_1.Cos(R_2).\left(Obest_i - x_i(t)\right)) \quad \dots (22)$$

where t is a transfer operator that changes the search focus from exploitation to exploration. $Obest_i$ Is described as the object's ideal final location. Random numbers in the range (0, 1) were designated as R_2 and R_1. Random numbers between zero and one were designated as C1 and C2, respectively. The search performance is improved by this transfer operator, which also manages the ratio of the local search in subsequent iterations to the global search in the initial iterations. Typically, the transfer function decreases and can be calculated using the following formula

$$T = 100X(-20X\frac{T}{T_{Max}}) \quad \dots (23)$$

Here, the maximum number of iterations is denoted byT_{Max}.

3.5 Step Size Limitation

Every iteration of the method works by controlling the distance that each object travels in each dimensional problem. The objects can handle wider cycles in the issue space owing to their stochastic variable step size. A necessary gap is designed for the object clamp movement associated with, in order to prevent these oscillations and to lessen divergence and explosion.

$$-S_{TMax} \le S_{Ti} \le S_{TMax} \quad \dots (24)$$

Here, S_{TMax} is a defined maximum movement produced that characterizes the maximum variation of an item throughout an iteration while taking positional coordinates into account. The formulation of this process is as follows

$$S_{TMax} = 0.1X(UB_i - LB_i) \quad \dots (25)$$

3.6 Position Updating

During this stage, item travels to the global optimum in the search space associated with the equation below

O_i(T+1)= O_i(T)+ $S_{Ti}(T+1)$ … (26)

3.7 Termination Condition

This stage involved verifying the termination condition. Convergence occurred when the maximum number of iterations was reached. Ultimately, the best options are stored and considered for recognizing facial expressions. And a modification to the typical PSO is introduced. Figure 8 depicts the flowchart for the recommended PSO-based MPPT approach. The key steps are provided in the following phases.

3.7.1 Parameter Selection

The suggested systems transmit four particles. The DC-DC converter's duty cycle (d) represents particle position. The fitness value function defines the generated power (Ppv).

3.7.2 Initializing the PSO

Using the PSO approach, particles can be positioned in a predetermined location or randomly distributed in space. The particle can alternatively be reset based on a known GMPP. In this study, the particles are initiated on specified places that cover the search space P_{min}, and P_{max}, representing the converter's max and min limits of duty cycles, correspondingly. The values were chosen as 0 and 0.95.

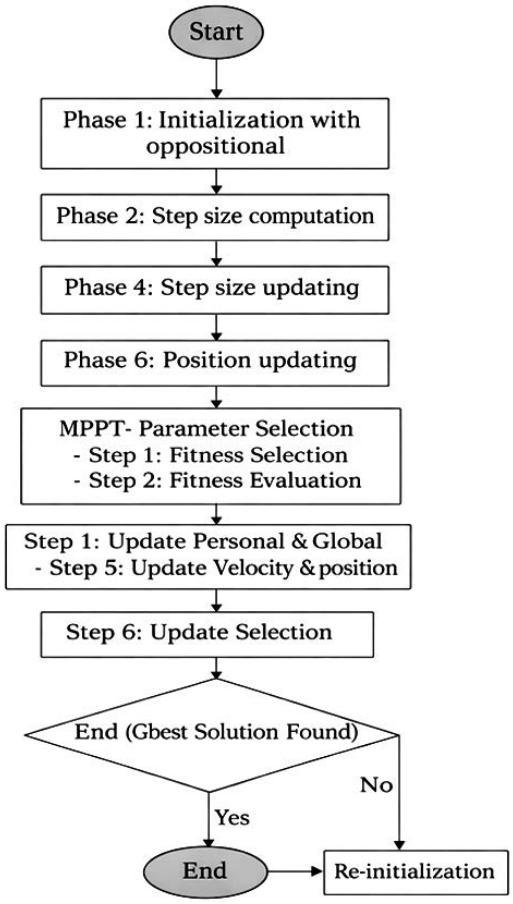

Fig. 8 — Flowchart for combined NCNN EGSA and PSO-MPPT algorithm

3.7.3 Fitness Evaluation

The PV output voltage signal and output current signals are detected and ciphered to determine the PV power output. This variable quantity can be utilized to calculate the i^{th} particle's fitness grade, P_{PV}.

3.7.4 Update Personal and Global Best Practices

A higher fitness grade particle P_{besti} becomes the new $P_{besti.}$ The particle with the highest fitness grade among all particles is selected as the new g_{best}. This is possible with the traditional PSO approach.

3.7.5 Update Each Particle's Velocity and Position

Following evaluation, all particles' new velocities and locations are updated. In a conventional PSO approach, the revision for velocities and locations is obtained using Eqs. (27-28).

$$\Delta d_i^{t+1} = \omega.\Delta d_i^t + c_1 r_1\left(P_{best_i} - d_i^t\right) + c_2 r_2\left(g_{best_i} - d_i^t\right) \quad \ldots (27)$$

$$d_i^{t+1} = d_i^t + \Delta d_i^{t+1} \quad \ldots (28)$$

The inertia weight x was set in the range of 0.4–0.9, with a linearly decreasing profile starting from 0.9 and reducing to 0.4, which provides an effective balance between global exploration and local exploitation. The cognitive coefficient c_1 and social coefficient c_2 were both chosen as 2.0, satisfying the convergence condition $c_1 + c_2 \leq 4$, which is commonly adopted in classical and recent PSO-based MPPT studies.

3.7.6 Convergence Evaluation

This paper utilizes two convergence standards. The method provides the $gbest$ solution when whole particle velocities are below a specific edge.

3.7.7 Re-initialization

Re-initialize particles based on environmental conditions.

Equation (29) detects environmental changes and triggers PSO re-initialization.

$$\frac{|P_{pv,new} - P_{pv,past}|}{P_{pv,past}} > \Delta P(\%) \quad \ldots (29)$$

4 Proposed System

4.1 System Description

A 100 kW PV system integrated with EV load connected to a 260V/25kV distribution network is designed in MATLAB/Simulink environment and parameters are tabulated in Table 2.

The developed PV+EV integrated system consists of a PV structure that generates DC power, which is regulated by a DC-DC converter and managed by PSO based MPPT controllers, a voltage source converter to convert DC-AC, allowing it to be used on the grid integrated and EV at the output side as presented in Fig. 9.

The tests were performed on different types of solar panel mismatches (partial shading, browning, and cracking) and on clean, dirty and shaded surfaces. From Fig. 10, At 0 s, the PV system has an initial output current of approximately 5.10 A, which corresponds to the initial discharge of the PV panel's electric charges due to the electromagnetic radiation of sunlight. The PV voltage equals 393.25 V; similarly, the DC voltage reads 587.05 V. These values indicate a stable point of operation, probably under good weather conditions, and therefore without shadowing.

For instance, when the time scale is 0.01 s, the PV current is slightly lower, 4.97 A, which might be a result of a small variation in the irradiance or ambient temperature, and the PV voltage increases to 398.55 V, which is the expected opposite behaviour in a PV system owing to the current-voltage curve of the solar cells. The DC voltage rises to 599.53 V, which could mean that there are some kinds of power electronics

Table 2 — Integrated PV and EV System Specifications

Parameter	Type/Rating	Symbol
Grid Specification	260 / 25	V/kV
PV System	100	kW
PV Panel	SP090P	-
Open Circuit Voltage	48	V
Short Circuit Current	10	A
Parallel Strings	2	-
Cells/Module	60	-
EV PMSM motor	50	kW
Number of Poles	4	-
Battery Nominal Voltage	350	V
Battery Current	60	A

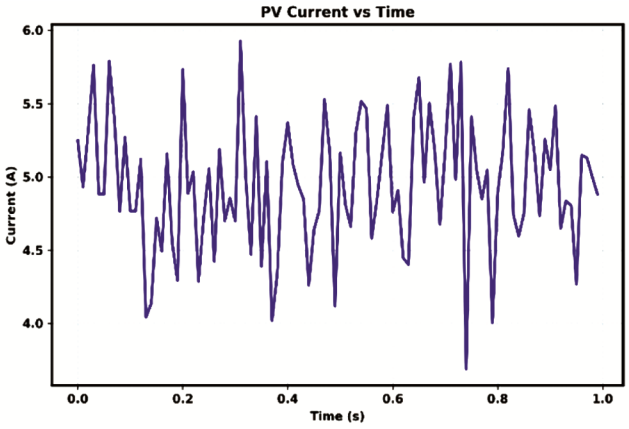

Fig. 10 — PV Current waveform

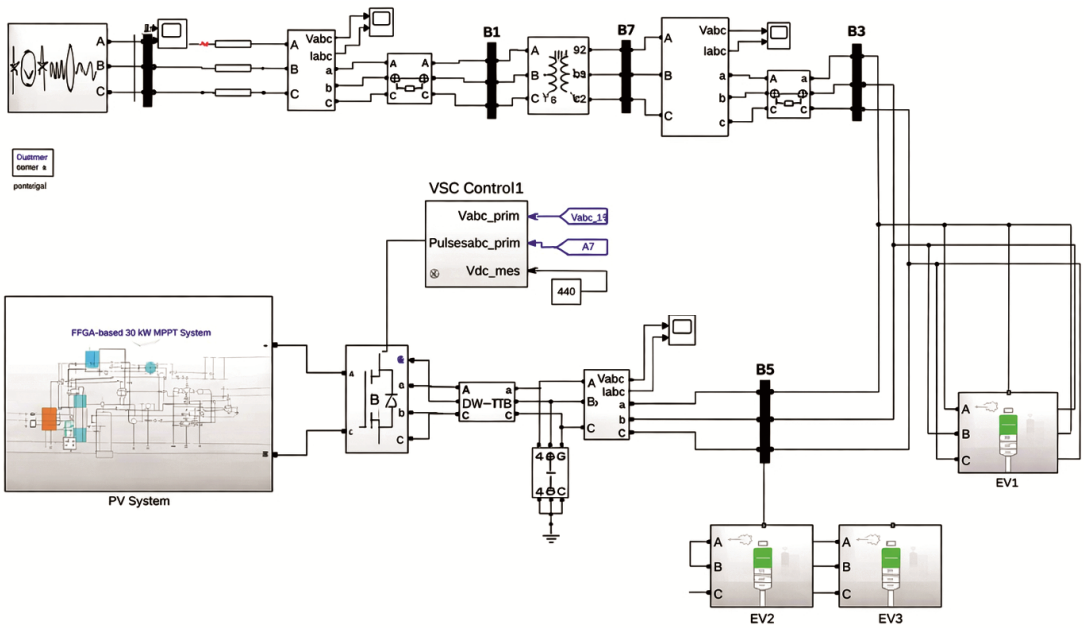

Fig. 9 — MATLAB/Simulink model of Proposed PV+EV integrated system

(PSO based MPPT algorithm of the inverter) that compensate and stabilize the power flow against small input changes. At 0.02 s, we observed PV current further increased to 5.13 A while PV voltage decreased to 392.08 V, indicating a real-time balance to maintain the MPP operation. The DC voltage at 600.27 V continues to stably increase, indicating that the PSO performs effective voltage regulation.

However, the PV current peaks at 5.30 A after 0.03 seconds, and the PV voltage increases to 396.92 V. Along with these changes, it indicates the presence of an increase in the solar irradiance or decrease in the cell temperature; either case will raise the current and voltage. DC voltage at 607.09 V also increases accordingly, showing that more energy is successfully harvested and balanced at the DC bus level.

Lastly, at 0.04 s, the PV current plummets to 4.95 A, and the PV voltage dips further to 402 V this would suggest a transient partial shading or decrease in solar intensity.

The DC voltage reaches 579.50 V, which indicates that the converter responds quickly to changes in the operating point and adjusts the output to keep the stability. The suggested NCNN-EGSA model performed exceptionally well in the identification of failure under partial shade, with just two false negatives and one false positive. Specifically, it accurately classifies 290 fault instances and 285 normal examples, showing good generalizability for both classes with minimal uncertainty. The confusion matrix's performance is shown in Fig. 11. The analysis of PSO based MPPT algorithm is made as follows, Initially, the structure was exposed to varying irradiance levels, as shown in Table 3. The PV output contains three MPPs, including GMPP placed on the right side. Figure 12 (a) displays the I-V curve for both GMPP and LMPP. Figure 12 (b) displays the GMPP attained at an output power value of P=527.6w. The proposed PSO algorithm achieved GMPP in 0.99s, with a PV output power of 518.27V. The P&O algorithm takes longer to reach GMPP 4.2s.

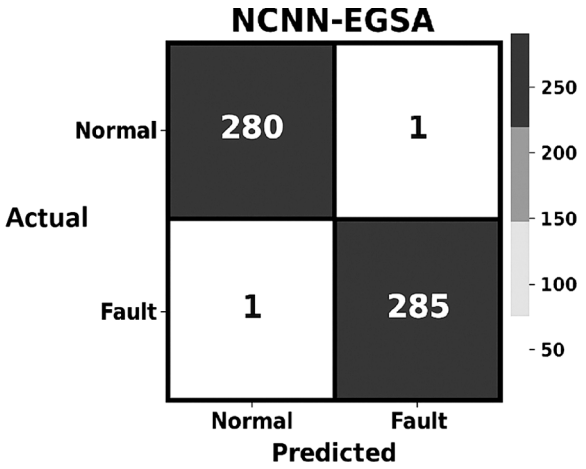

Fig. 11 — NCNN-EGSA Confusion Matrix

Nevertheless, in shadowing, standard P&O based MPPT approach have worse accuracy due to many local maxima. Figure12 (a) (with P&O) illustrates the inaccuracy of P&O based MPPT approaches under PSC. In this instance, the actual MPP is shifted at multiple points, alters duty points based on voltage command steps and oscillates. Power losses are also observed between the multiple peaks. The proposed PSO based MPPT technique address drawbacks of traditional models to avoid performance decrease, set MPPT to one peak power as shown in Fig. 12 (b) (with PSO).

Figures 13and 14 represents the three-phase grid voltages and three-phase grid's currents respectively for the PV+EV integrated system with the PSO based MPPT method. Address the advantage of developed models to avoid performance decrease.

The output voltage is regulated by the developed PSO based MPPT algorithm. The duty ratio is adjusted with the updated V_{max} and D_{max}, were improved compared with the P&O method. This

Table 3 — PV pattern

Parameter	Irradiance	Symbol
PV1	800	w/m^2
PV2	600	w/m^2
PV3	500	w/m^2
PV4	500	w/m^2

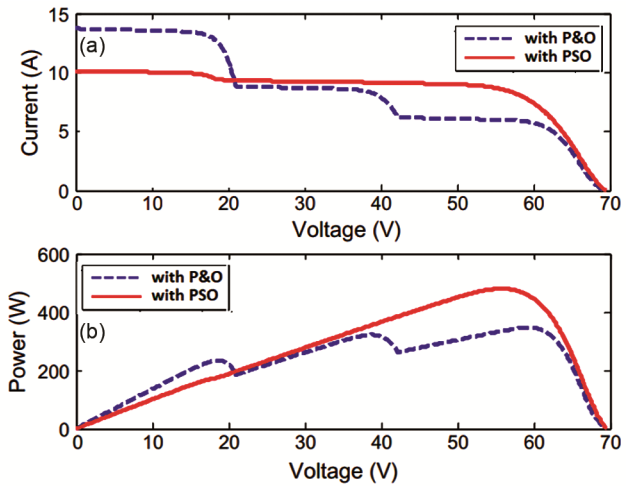

Fig. 12 — PV performance curves under PSCs with P&O and with PSO: (a) I-V characteristics and (b) P-V characteristics

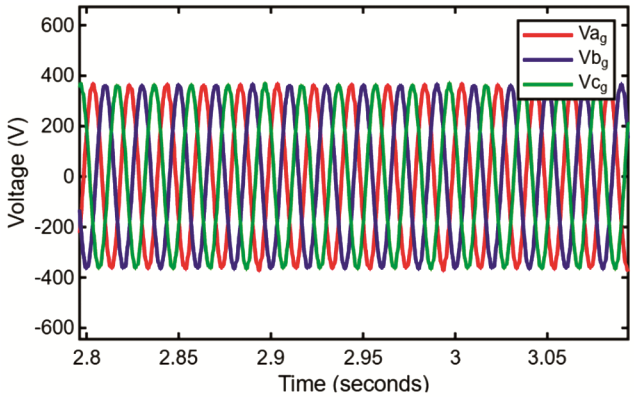

Fig. 13 — Three phase grid voltage

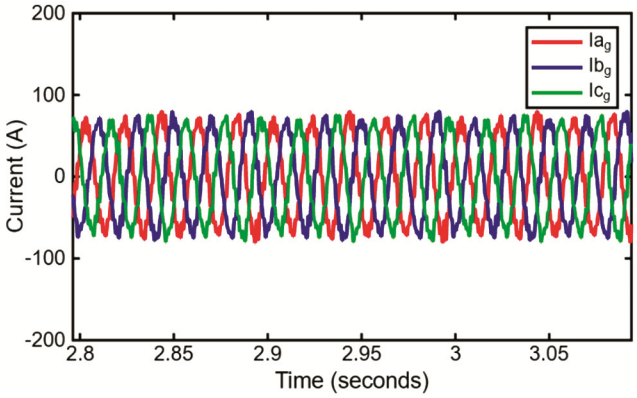

Fig. 14 — Three phase grid current

improvement be contingent on GMPP tracking, which provides faster convergence and precision improves overall PV performance.

5 Conclusion

The PV+EV integrated system and boost converter parameters are estimated, and MPPT tracking is implemented using the PSO Algorithm. The primary purpose of this work is to present a MPPT strategy based on the PSO Algorithm for monitoring the PV system's GMPP. The recommended PSO method may be carried out correctly under the PSC condition. Due to the PSC requirement, the standard P&O generates many peaks. As a result, the PSO algorithm is efficient, with a high convergence rate. The use of the PSO-MPPT algorithm is verified and analyzed under different operating scenarios. By the simulation results it is concluded that the proposed PSO based MPPT algorithm suits best for the PV+EV integrated systems. Future research will focus on hardware implementation using real-time controllers and experimental validation under practical operating conditions, as well as extending the framework to larger-scale grid-connected PV–EV systems.

References

1 Abdelsattar M, AbdelMoety A & Emad-Eldeen, *Neural Comput & Appl,* 37 (2025) 8825.
2 Khan M U I, Pathan M I H, Rahman M M, Islam M M, Chowdhury M A R, Anower M S, Rana M M, Alam M S, Hasan M, Sobuj M S I, Islam M B, Meena V & Benedetto F, *IEEE Access*, 12 (2024) 71566.
3 Aslam S, Kumar KV, Babu T A & Rajesh P, *Environ Dev Sustain*, 27 (2025) 1.
4 Ibrahim M H, Badran E A & Abdel-Rahman M H, *IEEE Access*, 12 (2024) 139199.
5 Atawi E, Hendawi E, Zaid S A, *Processes* 9 (7) (2021) 1246.
6 Hermans B, Walker S, Ludlage J, Ozkan L, *Appl Energy*, 368 (2024) 123210.
7 Zhang J, Sun K, Li C, Yang H, Zhou B, Hou X & Ge R, *Transp*, 15 (2023) 100209.
8 Nafeh A E-S A, Omran A E-F A, Elkholy A & Yousef H, *Result Eng*, 21 (2024) 101965.
9 Belhachat F, Larbes C, *Sol Energy*, 120 (2015) 399.
10 Pillai D S, Rajasekar N, Prasanth Ram J & Chinnaiyan V K, *Energy Convers Manage*, 178 (2018) 92.
11 Shami T M, El-Saleh A, Alswaitti M, Al-Tashi Q, Summakieh M A & Mirjalili S, *IEEE Access*, 10 (2022) 10031.
12 Mu A-Q, Cao D-X & Wang X-H, *Natural Sci*, 1 (2009) 151.
13 Cheikh-Mohamad S, Celik B, Sechilariu M & Locment F, *Appl Sci*, 13 (9) (2023) 5627.
14 Gogoi D, Bharatee A & Ray P K, *Electr Power Syst Res*, 229 (2024) 110113.
15 Secchi M, Barchi G, Macii D & Petri D, *Sustain Energy Grids Netw*, 35 (2023) 101120.
16 Kornelakis A, *Solar Energy*, 84 (2010) 2022.
17 Leitão D, Torres J P N & Fernandes J F P, *Energies*, 13 (19) (2020) 5017.
18 Silvestre S, Boronat A & Chouder, *Appl Energy*, 86 (9) (2009) 1632.
19 Chenni R, Makhlouf M, Kerbache T & Chenni A B, *Energy*, 32 (9) (2007) 1724.
20 Dhanabalan S & Ponnusamy T, *J Electr Eng Technol*, 20 (2025) 1747.